

Preparation of Boron by
Pyrolytic Decomposition of Boron Tribromide

by

Emily Thomas Lim

Department of Mechanical Engineering and Material Science
Duke University

Date: _____

Approved:

F. Hadley Cocks, Supervisor

W. Neal Simmons

Nico Hotz

Thesis submitted in partial fulfillment of
the requirements for the degree of Master of Science
in the Department of Mechanical Engineering and Material Science
in the Graduate School of Duke University

2016

ABSTRACT

Preparation of Boron by
Pyrolytic Decomposition of Boron Tribromide

by

Emily Thomas Lim

Department of Mechanical Engineering and Material Science
Duke University

Date: _____

Approved:

F. Hadley Cocks, Supervisor

W. Neal Simmons

Nico Hotz

An abstract of a thesis submitted in partial fulfillment of
the requirements for the degree of Master of Science in the
Department of Mechanical Engineering and Material Science
in the Graduate School of Duke University

2016

Copyright by
Emily Thomas Lim
2016

Abstract

The national shortage of helium-3 has made it critical to develop an alternative to helium-3 neutron detectors. Boron-10, if it could be produced in macroscopic alpha-rhombohedral crystalline form, would be a viable alternative to helium-3. This work has determined the critical parameters needed for the preparation of alpha-rhombohedral boron by the pyrolytic decomposition of boron tribromide on tantalum wire. The primary parameters that must be met are wire temperature and feedstock purity. The minimum purity level for boron tribromide was determined to be 99.999% and it has been found that alpha-rhombohedral boron cannot be produced using 99.99% boron tribromide. The decomposition temperature was experimentally tested between 830°C and 1000°C. Alpha-rhombohedral boron was found at temperatures between 950°C and 1000°C using 99.999% pure boron tribromide.

Dedication

I dedicate this thesis to my father for raising me to work hard in all that I do.

Table of Contents

Abstract.....	iv
List of Tables	viii
List of Figures.....	ix
Acknowledgements.....	xii
Chapter 1: Introduction.....	1
1.1 Crystal Structure.....	3
1.2 Application to Neutron Detectors.....	5
Chapter 2: Crystal Growth Methods for α -Rhombohedral Boron	8
2.1 Liquid Phase Solvent Growth.....	8
2.2 Gas Phase Pyrolysis Growth	9
2.3 Vapor-Liquid-Solid Phase Method.....	12
Chapter 3: Pyrolytic Decomposition.....	13
3.1 Experimental Setup	13
3.2 Procedure.....	19
3.3 Characterization Methods.....	22
3.3.1 Scanning Electron Microscopy	22
3.3.2 Energy Dispersive Spectroscopy.....	24
Chapter 4: Results and Discussion.....	25
4.1 Amorphous Boron.....	26
4.2 Alpha- and Beta- Rhombohedral Boron.....	32

4.3 High Vacuum Heating System	43
4.4 Boron Morphology Comparison.....	43
Chapter 5: Conclusions	47
Chapter 6: Future Work	48
Bibliography	50

List of Tables

Table 1: Parameters used in each pyrolytic decomposition experiment.....	21
Table 2: Mass of deposits and boron polymorphs found in experimental runs.	26
Table 3: Atomic and weight percent of elements in run 19.....	28
Table 4: Atomic and weight percent for run 24.	32
Table 5: Atomic and weight percent of elements in the brown clusters found in run 25.	35

List of Figures

Figure 1.1: An icosahedron of boron showing contours representing the concentration of bonding charge at each face and 12 boron atoms located at the vertices [3].	3
Figure 1.2: General unit cell of α -rhombohedral boron [4].	4
Figure 1.3: General unit cell of β -rhombohedral boron [4].	4
Figure 1.4: Schematic of solid-form semiconductor neutron detector consisting of a voltage source, ammeter, moderator, and neutron-to-ionizing radiation converter material in the form of α -rhombohedral boron.	7
Figure 3.1: Schematic of the boron tribromide pyrolysis system.	14
Figure 3.2: CAD drawing of the reactor assembly.	15
Figure 3.3: Boron tribromide pyrolysis system.	15
Figure 3.4: Diagram of boron tribromide flask setup.	18
Figure 3.5: Diagram of power feedthrough setup.	19
Figure 3.6: Heated wire during boron tribromide pyrolysis experiment.	19
Figure 3.7: Simplified schematic of a SEM system. Adapted from Stokes [22].	24
Figure 4.1: Optical microscopy images of (a) run 18 and (b) run 19.	27
Figure 4.2: SEM images of run 19 showing the (a) overall lumpy surface with (b) additional nodal clumps, potentially representing amorphous boron and tantalum boride respectively.	27
Figure 4.3: XRD pattern of sample 19 showing TaB_2 peaks and broad amorphous boron peak around 18 deg. XRD work was performed by David Rosenberg [21].	28
Figure 4.4: EDS spectrum for run 19.	28
Figure 4.5: OM images of run 23 showing the accumulation of gray amorphous boron and black lumps which may indicate another type of amorphous boron or TaB_2 .	29

Figure 4.6: OM images of run 24 showing darker gray deposits with slight luster and black spherical lumps.....	30
Figure 4.7: SEM images of run 24 showing the (a) gray lumpy base surface and the (b) spongy texture of the black spherical lumps.	31
Figure 4.8: XRD pattern of run 24 showing TaB ₂ peaks and broad amorphous boron peak around 18 deg. XRD work was performed by David Rosenberg [21].....	31
Figure 4.9: EDS spectrum for run 24.	31
Figure 4.10: OM images of run 25 showing the speckled, shiny gray deposit and light brown clusters.	33
Figure 4.11: SEM images of run 25 showing the microstructure of the (a) speckled gray material and (b) light brown clusters (1000x). (c) A 10000x magnification reveals angular particulates, suggesting crystalline α -B consistent with XRD findings.	34
Figure 4.12: XRD pattern of the brown clusters found in run 25 showing amorphous boron, TaB ₂ , and α -B. XRD work was performed by David Rosenberg [21].....	34
Figure 4.13: EDS spectrum for the brown clusters found in run 25.....	35
Figure 4.14: OM images of run 26 showing shiny gray deposit, similar to run 25 but with no speckled pattern.....	36
Figure 4.15: SEM images of run 26 at 1000x and 10000x magnification showing the (a) lumpy texture of the gray deposit and (b) smaller round particulates.	36
Figure 4.16: OM images of run 27 showing rough brown and gray deposits.....	38
Figure 4.17: SEM images of run 27 showing (a) the microstructure of the overlying brown deposit (1000x), (b) a cross section of the deposit (94x), and (c) the texture of the underlying gray deposits revealed in the cross-section (1000x).....	38
Figure 4.18: OM images of run 28 showing a shiny gray surface with an overlying layer of dull, darker gray material.	39
Figure 4.19: SEM images of run 28 showing (a) 103x overview of wire deposit, (b) lumpy texture of shiny gray material (1000x), and (c) spherical cluster structure of overlying dull gray material (1000x).....	40

Figure 4.20: Heated wire during run 29 showing an uneven accumulation of deposit, resulting in a non-uniform heat distribution.	41
Figure 4.21: OM images of run 29 showing (a) an overall rough gray surface with a few brown growths and (b) underlying shiny boron, as seen through the cracks.	42
Figure 4.22: SEM images (500x and 10000x) of run 29 showing the microstructure of the (a) rough gray material and (b) brown growths.....	42
Figure 4.23: High vacuum system for reheating pyrolytic decomposition samples to test for increased α -B growth.	43
Figure 4.24: Comparison of amorphous boron sample by Kuhlmann et al. [24] and sample 29 from the boron tribromide pyrolysis experiment.	44
Figure 4.25: SEM image of amorphous boron sample with 5-6% β -B by Kuhlmann et al. [24], showing angular crystals within the spherical cluster structure.....	45
Figure 4.26: Comparison of amorphous boron sample by Otto [25] and sample 25 from the boron tribromide pyrolysis experiment.	46
Figure 4.27: Comparison of alpha-rhombohedral boron growth from lumpy amorphous boron between sample by Otto [25] and sample 25.	46

Acknowledgements

Dr. Franklin Hadley Cocks is a man of many stories. Whether it is about science or life, every conversation I have had with him has taught me something new and valuable. His passion for his work and dedication to helping students are both motivating and humbling. I am lucky to have had the opportunity to work under his guidance, and I am thankful for every word we have exchanged.

Dr. Walter Neal Simmons has advised me throughout my entire undergraduate and graduate career at Duke. I have learned from him, worked under him, and worked with him on a variety of projects which have shaped me into the engineer I am today. His broad knowledge and diverse set of skills have influenced my perspective on what it means to be an engineer. My education would not have been the same without him.

Dr. Cocks and Dr. Simmons are more than just professors; they are truly great friends. By their example, they have taught me the importance of living to learn as opposed to learning to live. They have been supportive through hard times and have encouraged me to persevere. For that, I am incredibly grateful.

I would also like to thank David Rosenberg for all the years of working hard together through college and graduate research. His drive and commitment to his work are commendable. The past 5 years have been a long journey but I am glad I was able to experience it with him.

Chapter 1: Introduction

There is a growing concern of national security in the United States pertaining to the transportation of nuclear materials into the country for terrorist activity. Radiation portal monitors have been positioned around the borders to screen for nuclear materials by detecting neutron radiation. The main basis of neutron detectors is helium-3 (^3He). ^3He is produced as a byproduct of the radioactive decay of tritium, but the U.S. ceased tritium production in 1988. In 2008, the U.S. government became aware of the rapid shortage of ^3He and has since searched for alternative detector technologies [1]. The main alternatives being developed are boron-lined proportional detectors, boron trifluoride gas proportional detectors, and lithium-6 scintillator detectors. All three detectors, however, do not provide as high sensitivity as found in ^3He based detectors. A more effective semiconductor solid state neutron detector has been proposed using alpha-rhombohedral boron as the semiconducting material. This detector is estimated to provide more than 100 times greater sensitivity, on a unit volume basis, than currently available semiconducting and high pressure gas sensors and, if successful, is the most viable option [2].

Only one boron polymorph possesses unique semiconducting properties which are suitable for applications in neutron detection. The development of neutron detectors based on alpha-rhombohedral boron would make a major contribution to solving the

impending natural shortage of ^3He . The large nuclear cross-section of ^{10}B allows for more absorption of incoming neutrons and increased ionizing radiation in the form of ^7Li and α particles for higher measurement sensitivity. The reaction that drives this process is given as:



Natural boron only contains 19.6% ^{10}B , but boron enriched to 100% ^{10}B is commercially available. Many studies have thus been dedicated to using enriched boron in neutron detectors. Among the boron polymorphs studied, beta-rhombohedral boron ($\beta\text{-B}$) is the only crystalline form that can be consistently reproduced in substantial quantities. $\beta\text{-B}$, however, is a poor material for neutron detectors due to its high trap density and low charge mobility. As a result, when ^{10}B reacts with the incoming neutron flux and creates alpha particles which create electron-holes, these charges are unable to reach the measuring circuit if $\beta\text{-B}$ is used [2]. A more suitable yet rare form of crystalline boron is alpha-rhombohedral boron ($\alpha\text{-B}$). Unlike $\beta\text{-B}$, $\alpha\text{-B}$ is known to be a good semiconductor. The difficulty then lies first in producing $\alpha\text{-B}$ and second, in forming large enough crystals for implementation into a neutron detector. The purpose of this research is to determine the critical experimental parameters necessary for producing $\alpha\text{-B}$ through the pyrolytic decomposition of boron tribromide (BBr_3).

1.1 Crystal Structure

α - and β -rhombohedral boron share a common icosahedron structure with 12 boron atoms located at the vertices, as shown in Figure 1.1. The bonding associated with the icosahedron involves the three electrons from the second shell of each boron atom. Two of the electrons contribute to the internal bonding of the icosahedron whereas the third electron contributes to any external bonding. The strength of the internal bonds account for the material's high melting temperature [3].

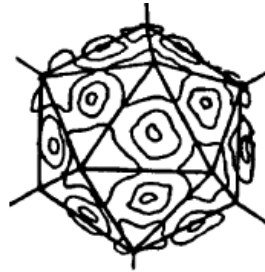


Figure 1.1: An icosahedron of boron showing contours representing the concentration of bonding charge at each face and 12 boron atoms located at the vertices [3].

The α -rhombohedral boron unit cell takes the shape of a distorted cubic close packing structure where each vertex is occupied by an icosahedron, illustrated in Figure 1.2. It is the simplest polymorph, containing only 12 atoms within the primitive unit cell. The bonds between the icosahedra within a boron lattice include two-electron bonds as well as three-centered δ bonds; it is the weak δ bonds that explain the transition of α -B to β -B at higher temperatures [4].

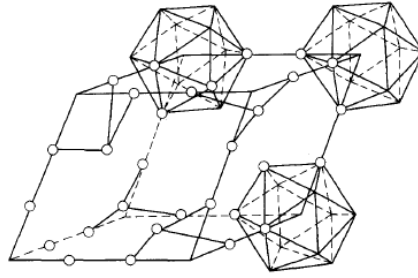


Figure 1.2: General unit cell of α -rhombohedral boron [4].

The β -rhombohedral boron unit cell follows a similar shape as the α -rhombohedral boron unit cell, but the B_{12} icosahedrons formerly centered at the vertices are replaced by B_{84} units. B_{84} units are made up of B_{12} icosahedra in the structural form $B_{12}(B_6)_{12}$. The remaining space in the center of the unit cell is occupied by a small chain of boron atoms in the structural form B_{10} -B- B_{10} . The β -B unit cell is shown in Figure 1.3. Although there are many atoms in the β -B unit cell, totaling to 105 boron atoms, the packing of the B_{84} units and inner boron atoms leaves considerable space within the cell and results in a loose structure [4]. The loose structure increases the number of interstitials and vacancies in the material which impedes the carrier mobility of β -B.

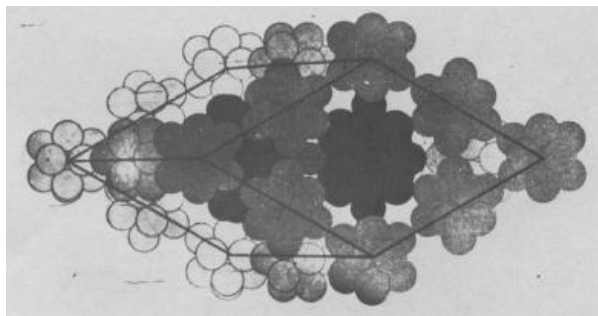
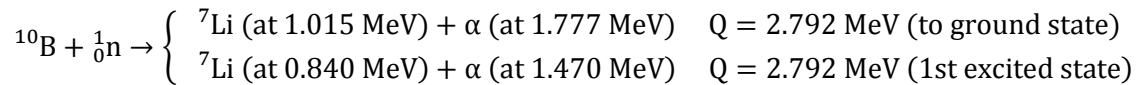


Figure 1.3: General unit cell of β -rhombohedral boron [4].

1.2 Application to Neutron Detectors

Solid state semiconductor neutron detectors are favored for their compactness and low-power operation but have thus far been limited in their sensitivity as compared to pressurized ^3He detectors. Semiconductor neutron detectors consist of two types: thin-film coated diode detectors and solid-form detectors. Thin-film coated diode detectors have thin layers of neutron reactive material applied to the surface of a semiconductor diode. The neutron interactions take place in the thin film and release ionized particles into the adjacent semiconductor diode to produce electron-hole pairs. In contrast, solid-form detectors utilize a neutron reactive material as the semiconductor diode itself, so the neutron interactions take place directly in the detector component. The disadvantage of thin film coated detectors is the self-absorption of reaction products that occurs within the outer film, resulting in less electron-hole pairs and decreased sensitivity [5]. Having the neutron reactions occur directly in the semiconducting material increases the probability of creating electron-hole pairs from the released products and, therefore, has motivated this research to develop a good semiconducting, neutron reactive material for solid-form neutron detectors.

Neutron detectors today most commonly implement either $^6\text{Li}(n,\alpha)^3\text{He}$ or $^{10}\text{B}(n,\alpha)^7\text{Li}$ reactions. Since the ^3He resource is rapidly diminishing, focus is placed on developing boron based semiconductor neutron detectors which implement the latter. The $^{10}\text{B}(n,\alpha)^7\text{Li}$ reactions are divided into two reactions:



where 94% of the reactions produce ${}^7\text{Li}$ at its first excited state and 6% produce ${}^7\text{Li}$ ions directly at its ground state. The excited ${}^7\text{Li}$ ions are quickly de-excited to their ground state by releasing a 480 keV gamma ray. The nuclear cross-section of ${}^{10}\text{B}$ for the absorption of thermalized neutrons is 3840 barnes [6].

The design of a solid state boron neutron detector must consist of a voltage source, ammeter, moderator, and neutron-to-ionizing radiation converter material. The moderator is needed to thermalize the neutrons, or to slow down the fast neutrons so they can be more readily absorbed by the semiconductor material. Once the thermal neutrons have been absorbed and reacted, the released ${}^7\text{Li}$ ions and α particles create a series of electron-holes pairs. An applied voltage then drives the free charges to their respective electrodes to produce a change in current which can be measured with an ammeter, or nanoammeter if necessary. For this study, the goal is produce α -rhombohedral boron to be used as the converter material. A schematic of the semiconductor neutron detector is shown in Figure 1.4.

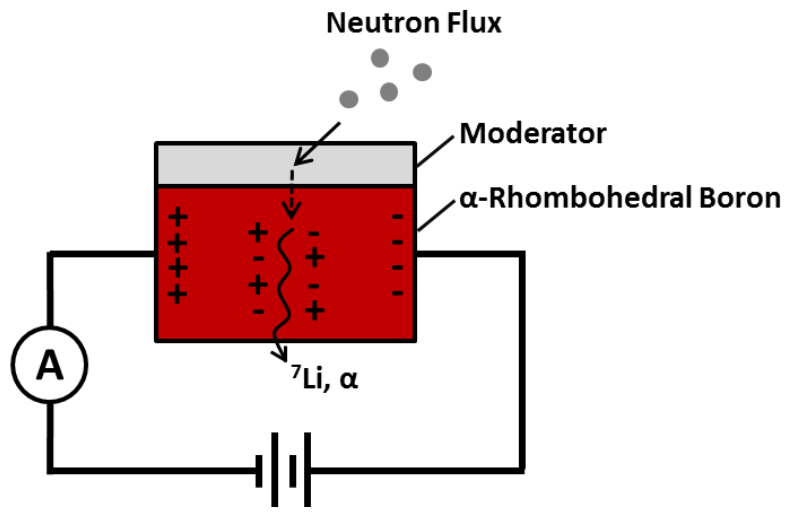


Figure 1.4: Schematic of solid-form semiconductor neutron detector consisting of a voltage source, ammeter, moderator, and neutron-to-ionizing radiation converter material in the form of α -rhombohedral boron. Df

Chapter 2: Crystal Growth Methods for α -Rhombohedral Boron

The first report of α -rhombohedral boron formation dates back to 1958 when McCarty *et al.* [7] discovered red glassy, microcrystalline material during the pyrolytic decomposition of BI_3 at 1000°C . Many methods have since been investigated to produce the unique α -B material. The main methods include liquid phase solvent growth, gas phase pyrolysis growth, and hybrid vapor-liquid-solid growth. The liquid phase solvent growth method involves precipitating solid boron from a liquid metal solvent whereas the gas phase pyrolysis method involves high temperature decomposition of gaseous boron compounds onto a substrate. The hybrid vapor-liquid-solid phase method is a combination of the two methods, using a liquid metal droplet as a nucleation site for boron to deposit from the vapor phase. The following sections review the methods in further detail and outline the major findings from each approach.

2.1 Liquid Phase Solvent Growth

The first success at forming α -B based on the liquid phase solvent growth method is attributed to F. Horn [8], who crystallized α -B from a boron-platinum melt. He determined the eutectic temperature of boron-platinum to be $825 \pm 5^\circ\text{C}$ and slowly cooled an alloy of 50 at. % B from 1200°C to the eutectic temperature until the melt solidified. The largest α -B crystals found were only tenths of millimeters in length, too small to allow for electrical and optical measurements to characterize their properties.

Attempts to find other possible, or even more suitable, solvents were made by F. Wald. F. Wald [9] found α -B in Cu, Au, Ag, Pt, and Pd solvents as well as in Au-Ge and Cu-Ni alloys after annealing at ~ 900 - 1020°C over ~ 1 - 2 months' time. In recent thesis work, Wei Gao [10] experimented with liquid phase growth of α -B using copper as the solvent. Copper was chosen for its low eutectic temperature, absence of intermediate phase boride compounds, ease of removal through nitric acid etching, and relatively low cost compared to other solvents. The largest α -B crystals produced were 500 microns in maximum length.

2.2 Gas Phase Pyrolysis Growth

Gas phase pyrolysis can produce α -B by decomposing boron halogenides or diborane onto heated substrates such as tantalum, boron nitride, and other boron filaments [11]. Early experiments by McCarty [12] involved the decomposition of purified boron triiodide (BI_3) onto ~ 0.075 mm diameter tantalum rods in a quartz reactor to produce red α -B at 800°C , 900°C and 1000°C up to 0.25 mm in size. The BI_3 was purified by distillation in a glass column to reduce the amount of unreacted iodine. X-ray powder diffraction (XRD) identified α -B at all three temperatures but only the 900°C and 1000°C samples showed red, glassy crystals that were visible to the unaided eye. For the purpose of this study, it is also important to note the appearance of the material surrounding α -B because it may help to identify precursor characteristics of α -B growth. The 800°C sample consisted of black, flaky material that contained mostly tantalum

boride (per XRD). The sample at 900°C had an exterior of dull, matte-like texture with a brownish, slightly purple hue and a few metallic, hemispherical growths. The center of the growths were dark colored and glassy, as seen from a top view, and the cross section revealed a glassy layer of clear red material, as seen within a fracture in the deposit. XRD results showed less tantalum boride in the 900°C deposit than in the 800°C run. The 1000°C produced the largest crystals of 0.25 mm, but they consisted of both red and black α -B, as identified by XRD. The black α -B possessed significantly different electrical resistivity behavior across temperatures and is assumed to have more impurities than the red α -B [13]. This research is interested in the most pure form of α -B for its use in semiconductor neutron detectors and will be referred to as red boron.

Further BI_3 pyrolysis experiments were conducted by Amberger and Dietze [14]. BI_3 was purified by zone-melting and decomposed at temperatures ranging from 850-1100°C onto tantalum wires of diameter 0.1-2.0 mm. Red boron was successfully produced within these parameters and, in contrast to McCarty's findings, the experiments showed no influence of temperature on the formation of α -B between 850-1100°C. Amberger and Dietze also carried out pyrolysis experiments using BBr_3 and BCl_3 , but no α -B was found. Overall, their results showed a strong dependence on purity for the formation of α -B, where non-zone-melted BI_3 seldom produced α -B compared to the zone-melted source. More impurities were believed to produce tetragonal and β -boron instead. Slightly greater amounts of α -B were formed on the larger diameter

wires, but the effects were attributed to less impurity diffusion due to uniform heating as opposed to greater surface area for the deposit. Based on their observations, Amberger and Dietze suggest that a thin layer of TaB₂ initially deposits onto the wire and allows glassy boron to accumulate on the surface. They believe it is the glassy boron that provides a growth site for α -B in the temperature range of 950-1100°C. The α -B found between 850-950°C was thought to have grown from the present tetragonal boron.

α -B formation by the pyrolytic decomposition of BBr₃ was studied by a number of scientists. Naslain et al. [15] performed the reaction in a quartz tube heated to 700-850°C in a resistance furnace, capping the maximum temperature at 850°C due to the silicon contamination. Results showed α -B growth within the entire temperature range and a dependence on a critical deposition time in which α -B forms without the presence of β -B. The critical time is dependent on the reactor geometry and is, therefore, not a practical parameter to estimate for different setups but should be kept in consideration when evaluating results. Other studies by Talley et al. [16] and Bean and Medcalf [17] showed α -B formation at temperatures as high as 1310°C and 1000°C, respectively, although both used different substrate materials (tungsten and β -B). Extensive research on the pyrolytic decomposition of BBr₃ was done by Wald and Bullitt [18]. 60 runs were performed in a mostly glass system with 99.999% pure BBr₃ over a temperature range of 995-1370°C. Black amorphous boron was found at temperatures below 1170°C and β -B was found at temperatures from 1170 to 1370°C. Observations suggested that red α -B

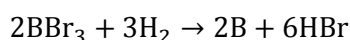
nucleated from amorphous boron at temperatures between 1150-1220°C when the system purity was sufficient. The largest red boron crystals formed were ~0.1 mm in size. The system presented in this thesis is modeled after the Wald and Bullitt system with modifications to the reaction chamber and lines.

2.3 Vapor-Liquid-Solid Phase Method

The general vapor-liquid-solid phase method was developed by Wagner and Ellis [19] in application to silicon crystal growth. The idea was to use a liquid metal or alloy droplet as a preferred site for deposition from a vapor compound. The deposits would then crystallize, grow, and precipitate out of the liquid droplet. Sitarik and Ellis [20] combined this method with the pyrolysis of BCl_3 to produce microcrystalline fibers of red boron. In a fused silica open tube, hydrogen carried BCl_3 vapor over a heated substrate on which liquid platinum particles were scattered. At ~1000°C, red boron whiskers of 2 mm in length and 25 μm in cross section were grown.

Chapter 3: Pyrolytic Decomposition

The goal of this research is to grow alpha-rhombohedral boron (α -B) by the pyrolytic decomposition of boron tribromide. Boron tribromide can be reduced by hydrogen at elevated temperatures to produce and deposit boron onto a heated tantalum wire, following the reaction



The deposited boron takes the form of various polymorphs depending on the temperature of the wire and other factors such as impurity level, hydrogen flow rate, BBr_3 flow rate, and deposition time. Some experiments from literature show that the flow rate and deposition time have a significant effect on α -B growth whereas other experiments suggest that their effects are minimal. Overall, past experiments agreed that the temperature of the wire and amount of impurities in the system are the main contributors to α -B growth or the lack thereof. Therefore, this research has focused on the effect of pyrolysis conditions, especially wire temperature, on the decomposition of BBr_3 and the growth of α -B while attempting to minimize the presence of impurities in the decomposition process.

3.1 Experimental Setup

The pyrolytic decomposition of BBr_3 has been carried out in a stainless steel, 6-way KF (Klein Flange) cross apparatus made for ultra-high vacuum systems by the Kurt J. Lesker company, and is referred to as the reactor in the setup schematic shown in

Figure 3.1. The KF connections contain centering rings which hold o-rings made of fluorocarbon, a material known for its high chemical resistance. The 6 ports served different functions: the bottom port acting as a connection to a base stand, the top port acting as a power feedthrough for the tantalum wire, the 2 parallel ports allowing for hydrogen flow, and the 2 parallel viewports. The circuit to the right of the reactor connected to the hydrogen and helium tanks and BBr₃ flask, whereas the circuit to the left of the reactor connected to the vacuum pump, cold trap, and water bubbler. Check valves were strategically placed to control the direction of hydrogen flow through the circuits and provide easier troubleshooting of vacuum leaks. A CAD drawing of the reactor assembly is shown in Figure 3.2. The actual setup is shown in Figure 3.3, with lines leading to the hydrogen and helium tanks and temperature controller (unshown).

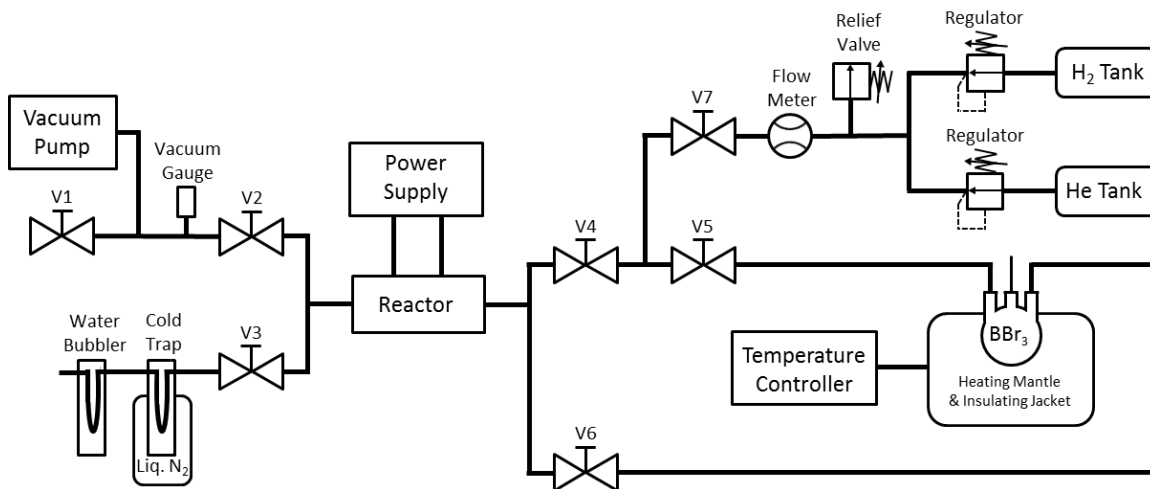


Figure 3.1: Schematic of the boron tribromide pyrolysis system.

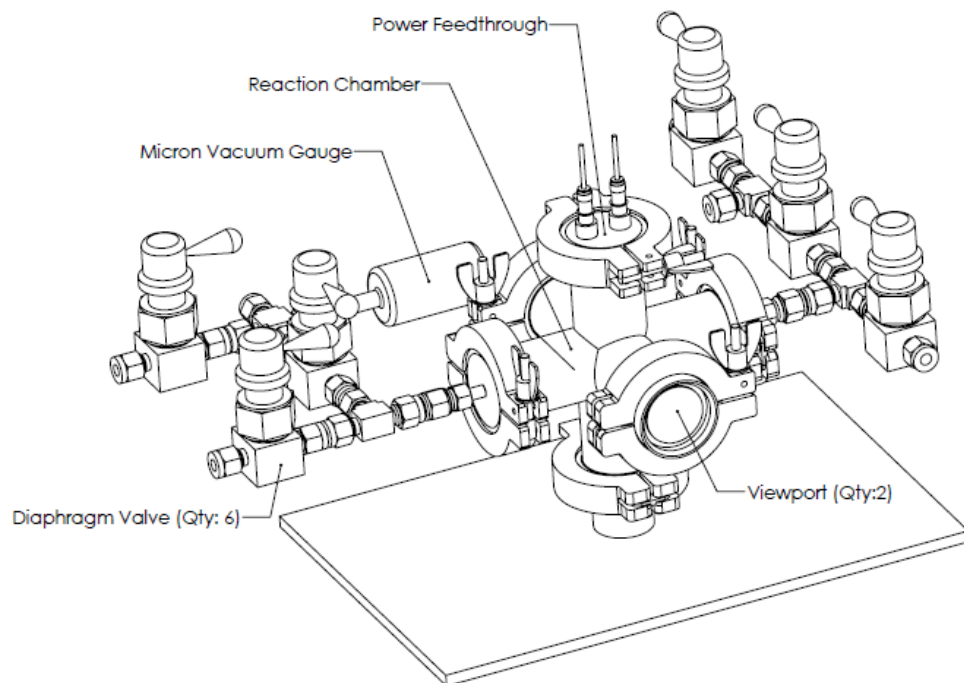


Figure 3.2: CAD drawing of the reactor assembly.

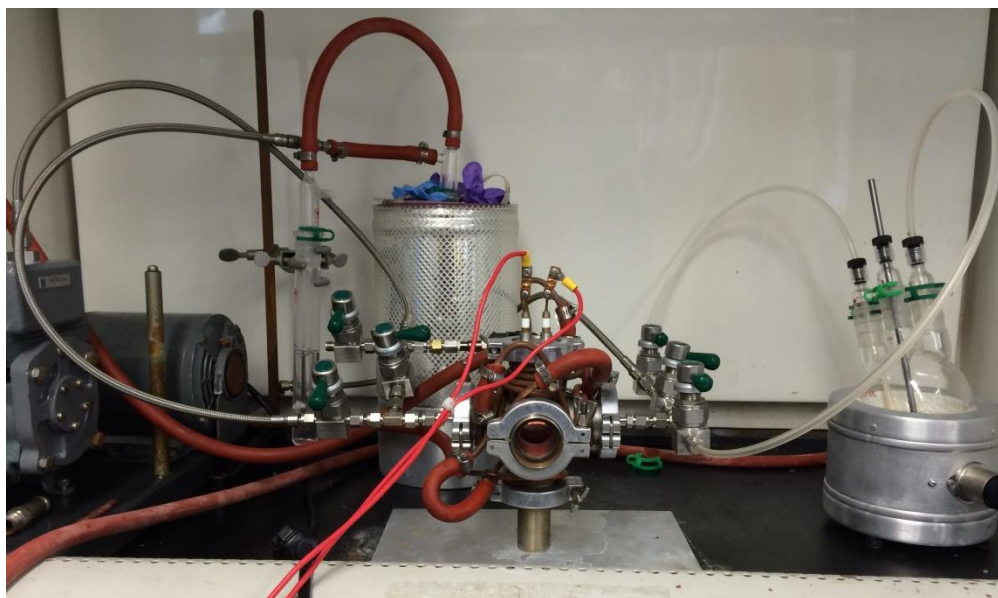


Figure 3.3: Boron tribromide pyrolysis system.

One important consideration in the design of the setup was minimizing impurities in the system. The lines consisted of mostly Teflon core and stainless steel braided tubing from Swagelok to prevent corrosion. Stainless steel tubing was used to connect valve 2 to the vacuum pump and valve 3 to the cold trap. Nonreactive Teflon tubing was used to connect the BBr_3 flask to the rest of the system through valves 5 and 6. A water bubbler was placed downstream of the reaction to prevent air from leaking back into the system and, in addition, for reacting any unreacted BBr_3 and hydrobromic acid for later disposal. The vacuum pump was able to remove most of the oxygen and water vapor from the reactor, BBr_3 flask, and lines leading up to valve 7 (V7). To help facilitate the evacuation, a heat gun was used to drive off excess water from the walls of the reactor and glass flask housing the BBr_3 . Additionally, all o-rings and flask stoppers were assembled with nonreactive silicon vacuum grease (Dupont Krytox Performance Lubricant) to better seal the connections. The resulting vacuum was ~50 microns.

The BBr_3 compound was contained in small sealed glass ampules which were loaded into a 3-neck round glass flask from Ace Glass. Due to the limited availability of BBr_3 , samples from different manufacturers were used, specifically 5g ampules rated at $\geq 99.99\%$ purity from Aldrich and 10g ampules rated at $\geq 99.999\%$ purity from Alfa Aesar. At first, only one 5g BBr_3 ampule was reacted in a 50mL round flask per experiment. When transitioning to the 10g BBr_3 ampule, the flask was switched out for a 500mL flask to allow room for the larger ampule. As shown in Figure 3.4, two ports were used as

feedthroughs for hydrogen to bubble through and carry the BBr_3 to the reactor. The middle port was used as a tool feedthrough, initially housing a stainless steel sharpened rod intended for breaking the BBr_3 ampule. Subsequently, a high purity tantalum rod was substituted for the stainless steel rod. This was done because the stainless steel rod showed visible corrosion from the hydrobromic acid. The flask could be isolated from the rest of the system through check valves while attempts were made to break the ampule. This would prevent risk of contaminating the wire in the event that leaks were introduced during the process. Breaking the ampule was difficult given the little support available to hold the ampule rigid when applying an impulse force through the tantalum rod. In some cases, the o-rings in the sealed feedthroughs became dislodged, or the tapered glass joints were pushed out with the excessive movement involved in breaking the ampule. The flask rested on a heating mantle to warm the boron tribromide during the experiment and increase mixing; a thermocouple and temperature controller was connected to maintain a temperature of $\sim 50^\circ\text{C}$.

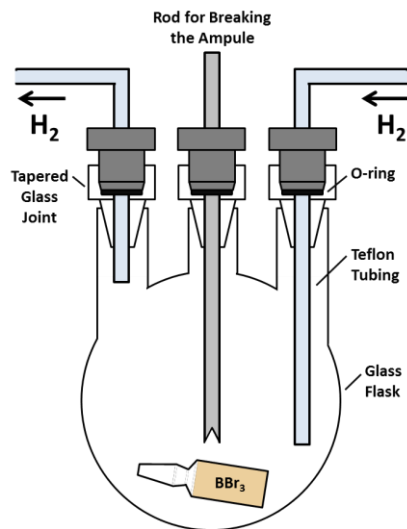


Figure 3.4: Diagram of boron tribromide flask setup.

The power feedthrough was designed using copper to provide an effective electrical connection with the tantalum wire. The setup consists of two copper rods with stainless steel adapters at the end to secure the U-shaped wire by a pair of set screws. A diagram of the setup is shown in Figure 3.5. A wire diameter of 1.0mm is used because it is the maximum size that can be heated to 1200°C with the available power supply, which is capable of supplying a maximum of 50A at 8V (Agilent 6651A). Larger diameter wire is recommended to allow thinner layers to build up and ensure a more uniform temperature distribution across the overall cross section. Thicker deposits require more heat to be generated in the wire to maintain the target temperature at the surface and, as a result, increases the diffusion of impurities from the tantalum wire to the surrounding boron deposit [14]. A picture of the heated wire during experimentation is shown in Figure 3.6.

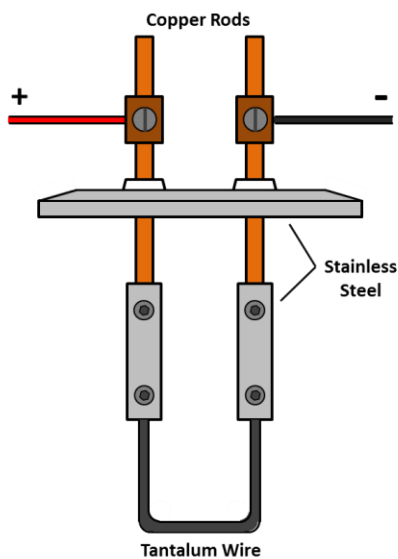


Figure 3.5: Diagram of power feedthrough setup.

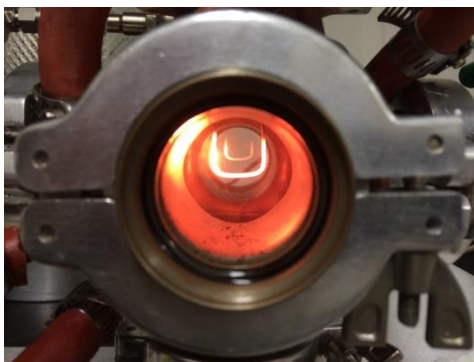


Figure 3.6: Heated wire during boron tribromide pyrolysis experiment.

3.2 Procedure

In preparation for each experiment, the tantalum wire was cleaned and weighed before mounting to the power feedthrough. The dewar for the cold trap was filled with liquid nitrogen to freeze excess boron tribromide and the downstream bubbler was filled with water to dilute the HBr byproduct. The BBr_3 ampule(s) were cleaned of their labels

and placed into the 3-neck flask. Once the setup was fully assembled and sealed, the vacuum pump began to evacuate the system. A heat gun was used to help drive off the remaining water left on the inner surfaces. The vacuum stabilized at ~50 microns. Assuming the system was vacuum limited at 50 microns, additional steps were taken to further reduce the amount of impurities. The system was flushed twice with hydrogen to help rid the chamber of residual oxygen and water, and the wire was heated with a small applied current in vacuum as a final attempt to drive off gas or water absorbed on its surface.

The experiment was ready to begin after the setup preparations were completed. Valve 2 (V2) to the vacuum pump was closed and the system was pressurized with hydrogen. When fully pressurized to 1.05 atm, V3 was opened to the cold trap and bubbler to allow continuous flow through the chamber. The glass flask was isolated by closing V5 and V6 while keeping V4 open. This was done in case leaks were introduced when breaking the BBr_3 ampules in the flask. The tantalum rod was used to secure the ampule against the wall of the flask and allow an impulse force to be applied from the outside to break the glass and release the BBr_3 .

The wire needed to heat up to temperature before opening the valves to the BBr_3 . A 50V power supply was used to apply the appropriate amount of current to reach the target temperature. The temperature was measured using an optical pyrometer (Spectrodyne DFP 2000). With the wire up to temperature, V5 and V6 were opened and

V4 was closed to ensure most of the hydrogen bubbled through the flask to mix with BBr_3 and carry these reactants across the hot wire. The Teflon tubing allowing hydrogen inflow to the flask was positioned lower to sit in the BBr_3 puddle for more direct mixing. The temperature was periodically checked every 10-20 min, and the current was increased to maintain the target temperature as more boron was deposited on the wire. The experiment continued to run until all of the BBr_3 was visibly gone. Table 1 lists the specific parameters used in each experiment. It is important to note that the actual wire temperature may be $\sim 50^\circ\text{C}$ hotter than the pyrometer reading depending on how much radiation is absorbed by the viewport glass. The temperatures shown in Table 1 are the measured pyrometer readings.

Table 1: Parameters used in each pyrolytic decomposition experiment.

Run Number	BBr_3 Ampules	BBr_3 Purity	Supplier	Max Current	Temp	Deposition Time
18	1 5g ampule	99.99%	Aldrich	35.2A	830°C	44min
19	1 5g ampule	99.99%	Aldrich	35.0A	830°C	43min
23	1 10g ampule	99.999%	Alfa Aesar	34.5A	830°C	2hr 33min
24	1 10g ampule	99.999%	Alfa Aesar	37.7A	900°C	2hr 4min
25	1 10g ampule	99.999%	Alfa Aesar	38.5A	950°C	2hr 14min
26	2 5g ampules	99.99%	Aldrich	40.0A	975°C	1hr 35min
27	1 10g ampule	99.999%	Alfa Aesar	43.3A	1000°C	2hr 2min
28	1 10g ampule	99.999%	Alfa Aesar	40.9A	975°C	2hr 18min
29	1 10g ampule	99.999%	Alfa Aesar	40.6 A	950°C	2hr 15min

The post-run procedure was designed to reduce the brittleness of the wire caused by the hydrogen diffusing into the tantalum wire. With the wire still up to temperature, the flask was closed off and the chamber was pressurized with helium instead of

hydrogen. Helium continued to flow across the wire for the same amount of time the hydrogen was used. The difference in heat transfer into helium compared to hydrogen required adjusting the current to maintain the target temperature. After the allotted amount of time, the power supply was turned off and the valves to the cold trap (V3) and helium tank (V7) were closed. The wire cooled in the helium pressurized chamber for ~10 min. Safety procedure included venting the system through V1 with the vacuum pump turned off and V2 open. The wire was dismantled and weighed for the mass of the deposit.

3.3 Characterization Methods

The boron deposits are characterized through optical microscopy (OM), scanning electron microscopy (SEM), energy dispersive spectroscopy (EDS), and x-ray diffraction (XRD). This thesis evaluates the pyrolysis results by appearance, as seen through optical microscopy and scanning electron microscopy. Collaboration with David Rosenberg [21] provided XRD identification of the deposits. Energy dispersive spectroscopy was used to help identify amorphous boron from tantalum borides in the samples where XRD revealed little to no crystalline boron. The following sections provide a brief overview of the different characterization methods performed for this study.

3.3.1 Scanning Electron Microscopy

Scanning electron microscopy utilizes a concentrated electron beam to charge particles on a specimen surface. The emitted particles are then collected and processed

to form images. Among the many types of electrons reflected, absorbed, and transmitted, SEM mainly uses backscattered electrons and secondary electrons. Backscattered electrons are electrons that are reflected back through the surface by a series of collisions with the specimen atoms. Secondary electrons are loosely bound valence electrons that have been excited to the extent of reaching the conduction band and propagating through the atoms; those that reach the specimen surface are emitted. High magnification images can be captured because the size at which features can be distinguished is based on the wavelength of the electrons within the incident beam. The wavelength of electrons is very small, being on the order of 10^{-11} m for a 30 kV accelerating voltage (voltage used for examining the experimental samples) [22].

A SEM system generally consists of an electron source, lenses and apertures for beam focusing, coils for beam scanning, a detector for signal collection, and a vacuum system. The vacuum is necessary to prevent contamination of the electron source and any scattering that may be caused by air [22]. A simplified schematic of a SEM system is given in Figure 3.7.

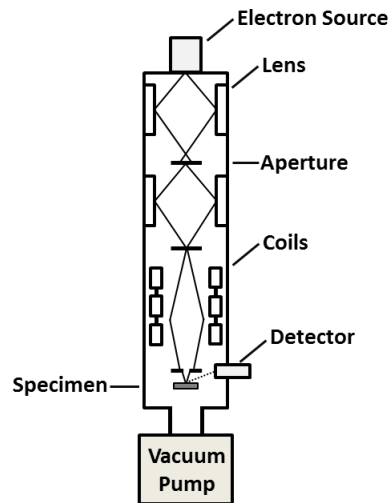


Figure 3.7: Simplified schematic of a SEM system. Adapted from Stokes [22].

3.3.2 Energy Dispersive Spectroscopy

Energy dispersive spectroscopy can be implemented in the same setup as scanning electron microscopy. EDS is based on the measurement of characteristic x-rays as opposed to emitted electrons. Characteristic x-rays are produced when an incident electron interacts with the tightly bound inner shell electrons of a specimen atom and ejects an electron. The excited atom then relaxes to its ground state by transitioning an outer shell electron to fill the inner shell vacancy. The energy produced by this phenomenon is the difference in energy of the electrons from the outer and inner shells. This energy may cause another outer shell electron to be ejected, or this energy could be emitted as a photon of electromagnetic radiation. In the event of the latter, the x-rays can be collected and measured to identify the chemical makeup of the specimen based on the energies characteristic to specific elements [23].

Chapter 4: Results and Discussion

The results of each run are summarized in Table 2, including the mass of the deposit and the boron compounds and polymorphs identified by x-ray diffraction. The x-ray diffraction results were determined by David Rosenberg [21]. This list begins with run number 18 because runs 1-17 were part of the initial apparatus refinement, involving failures of various kinds, e.g. wire breaking, excessive air contamination leading to oxidation, vacuum failure, etc. Runs 20-22 are not listed due to procedural errors leading to contaminated wires.

Based on the experimental data, purity played an important role in producing alpha rhombohedral boron, particularly in the temperature range of 950-1000°C. The higher purity 99.999% BBr₃ ampules from Alfa Aesar made α -B at 950°C and 1000°C whereas the lower purity 99.99% BBr₃ ampules from Aldrich did not make α -B at 975°C or in any of the first 22 runs. The temperature not only affected the type of boron formed on the wire but also the amount of material deposited. The higher the temperature, the more deposit accumulated onto the wire which, in turn, required higher current to maintain the target temperature at the surface of the deposit. The following sections provide optical microscope (OM) and scanning electron microscope (SEM) images of the material produced in each experiment and qualitative analysis on the parameters contributing to the formation of different boron polymorphs.

Table 2: Mass of deposits and boron polymorphs found in experimental runs.

Run Number	BBr ₃ Purity	Max Current	Temp	Deposition Time	Mass of Deposit	Boron Compounds and Polymorphs
18	99.99%	35.2A	830°C	44min	N/A	TaB ₂ , amorphous boron
19	99.99%	35.0A	830°C	43min	N/A	TaB ₂ , amorphous boron
23	99.999%	34.5A	830°C	2hr 33min	0.021g	TaB ₂ , amorphous boron
24	99.999%	37.7A	900°C	2hr 4min	0.056g	TaB ₂ , amorphous boron
25	99.999%	38.5A	950°C	2hr 14min	0.099g	TaB ₂ , α-B, amorphous boron
26	99.99%	40.0A	975°C	1hr 35min	0.112g	TaB ₂ , amorphous boron
27	99.999%	43.3A	1000°C	2hr 2min	0.166g	TaB ₂ , α-B, β-B, amorphous boron
28	99.999%	40.9A	975°C	2hr 18min	0.145g	TaB ₂ , β-B, amorphous boron
29	99.999%	40.6A	950°C	2hr 15min	0.137g	TaB ₂ , β-B, amorphous boron

4.1 Amorphous Boron

Amorphous boron appeared in the temperature range of 830-1000°C. Runs 18 and 19 at 830°C produced dark gray, opaque samples with lumpy surfaces, shown in Figure 4.1. Run 19 showed additional nodal clumps, which may be a result of more impurities in the system. A closer view of run 19 was taken through SEM, shown in Figure 4.2. XRD revealed signatures of amorphous boron and tantalum boride (TaB₂), consistent with the findings in other experiments at similar temperatures [12, 18]. It is difficult to discern from just the XRD pattern whether amorphous boron or TaB₂ is more

prevalent in the deposit. For example, Figure 4.3 shows the XRD pattern for sample 19, compiled by David Rosenberg [21]. The TaB_2 peaks are distinct whereas the broad amorphous peak around 18 deg is more subtle. The relative quantities cannot be determined by visibly comparing the two peaks. Thus, EDS was applied to quantify the atomic percent of boron vs tantalum and distinguish what the majority of the deposit was made of. Figure 4.4 shows the EDS spectrum and Table 3 shows the corresponding atomic percentages for run 19. The 97.47 at% of boron compared to 0.53 at% of tantalum found in the sample proves that the deposit contains mostly amorphous boron.

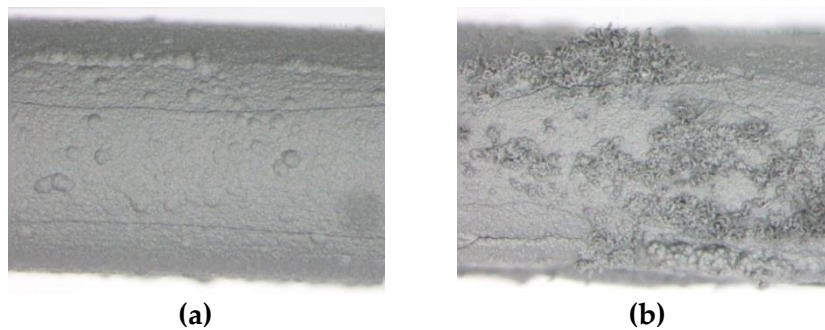


Figure 4.1: Optical microscopy images of (a) run 18 and (b) run 19.

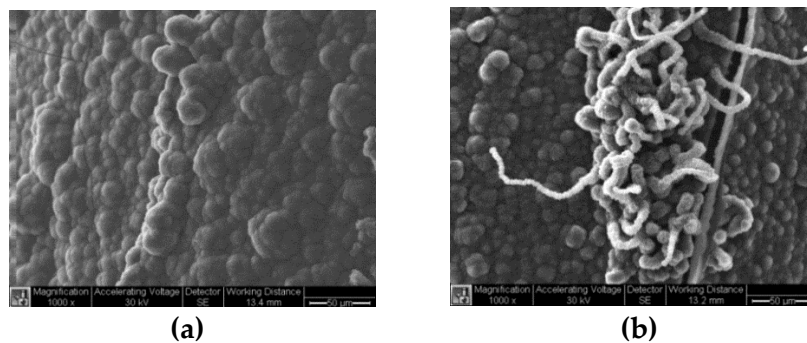


Figure 4.2: SEM images of run 19 showing the (a) overall lumpy surface with (b) additional nodal clumps, potentially representing amorphous boron and tantalum boride respectively.

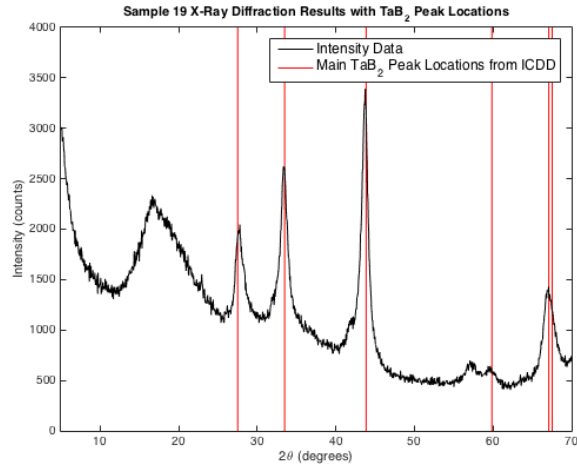


Figure 4.3: XRD pattern of sample 19 showing TaB₂ peaks and broad amorphous boron peak around 18 deg. XRD work was performed by David Rosenberg [21].

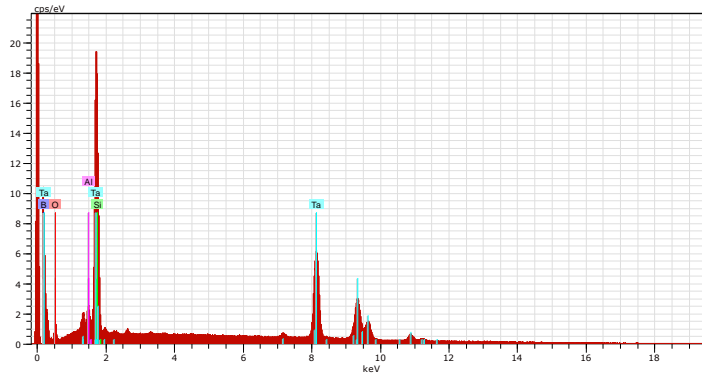


Figure 4.4: EDS spectrum for run 19.

Table 3: Atomic and weight percent of elements in run 19.

El	AN	Series	C norm.	C Atom. (1 Sigma)	[wt. %]	[at. %]	[wt. %]
B	5	K-series	49255	88.92	97.47	10.52	
O	8	K-series	10936	2.36	1.75	0.35	
Al	13	K-series	15629	0.24	0.11	0.04	
Si	14	K-series	24199	0.34	0.14	0.04	
Ta	73	L-series	234439	8.14	0.53	0.22	

Runs 18 and 19 used 5g BBr_3 ampules from Aldrich rated at $\geq 99.99\%$ purity. As a comparison, another experiment (run 23) was conducted at the same temperature of 830°C using a 10g ampule from Alfa Aesar rated at $\geq 99.999\%$ purity. Run 23 produced a similar gray lumpy base texture, suggesting amorphous boron. In contrast to runs 18 and 19, the sample also grew black spherical lumps on the exterior. See Figure 4.5 for OM images. The black material may be some form of TaB_2 , but given the 2hr 33min deposition time, it may also be a different form of amorphous boron which developed over a longer heating period (more than twice as long as runs 18 and 19). XRD again showed characteristics of amorphous boron and TaB_2 .

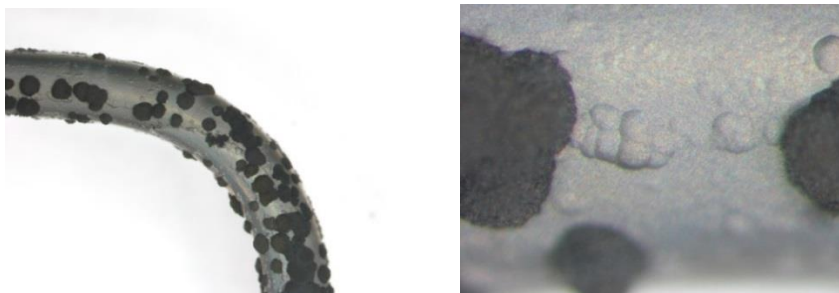


Figure 4.5: OM images of run 23 showing the accumulation of gray amorphous boron and black lumps which may indicate another type of amorphous boron or TaB_2 .

Using another 10g BBr_3 ampule from Alfa Aesar, the temperature was increased to 900°C for run 24 with the expectation of greater amorphous boron growth. The deposit consisted of darker shades of gray and less black spherical lumps, shown in Figure 4.6. The gray deposit also had more luster than that of runs 18, 19, and 23. XRD carried out by David Rosenberg [21] identified amorphous boron and TaB_2 . Figure 4.8

shows the corresponding XRD pattern. EDS analysis, depicted in Figure 4.9 and Table 4, revealed a 96.43 at% boron to 0.07 at% tantalum distribution, indicating that the deposit consisted almost entirely of amorphous boron. The shiny surface may indicate glassy amorphous boron as opposed to dull powder amorphous boron. Glassy amorphous boron is a precursor to α -B [14] and its presence would support the findings of crystalline α -B at higher temperatures in following experiments. SEM images of run 24 (Figure 4.7) show the same lumpy base texture as run 19 (Figure 4.2). The gray, lumpy appearance is likely characteristic of amorphous boron based on the observations made from runs 19-24. The SEM images also give a closer look at the spongy texture of the black lumps, which could be caused by impurities within the system. EDS results imply that these black spots are also amorphous boron, but they may be a more impure form.

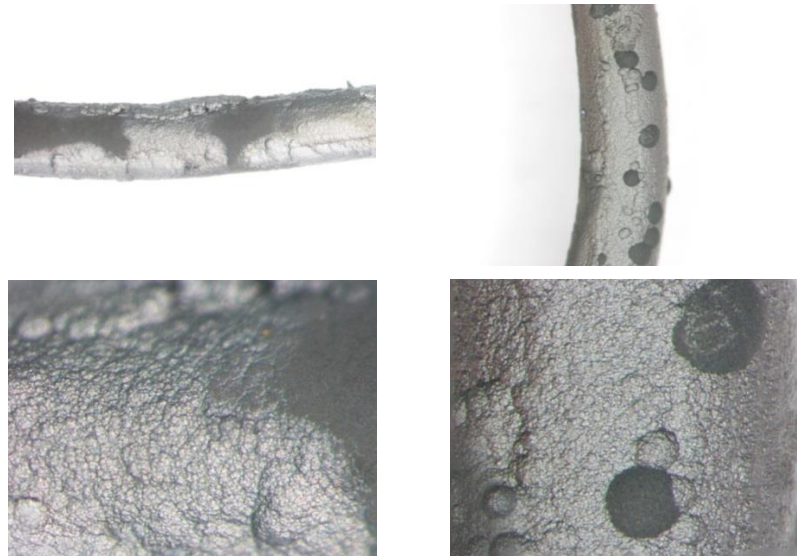


Figure 4.6: OM images of run 24 showing darker gray deposits with slight luster and black spherical lumps.

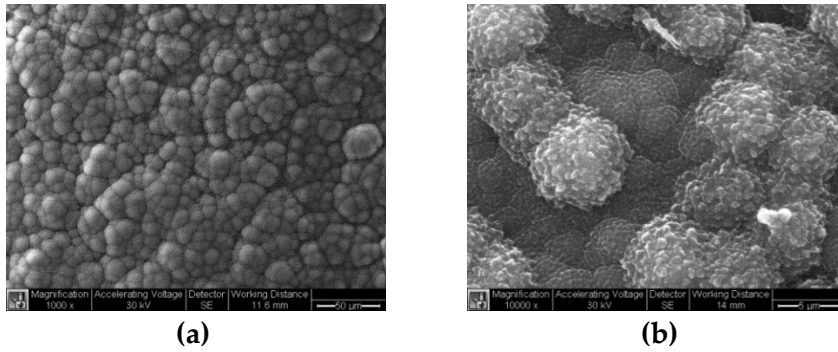


Figure 4.7: SEM images of run 24 showing the (a) gray lumpy base surface and the (b) spongy texture of the black spherical lumps.

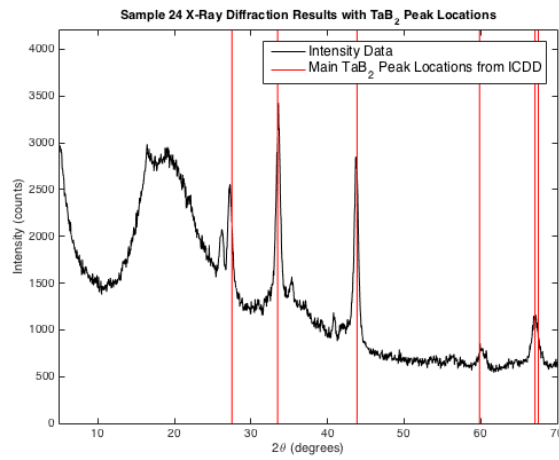


Figure 4.8: XRD pattern of run 24 showing TaB_2 peaks and broad amorphous boron peak around 18 deg. XRD work was performed by David Rosenberg [21]

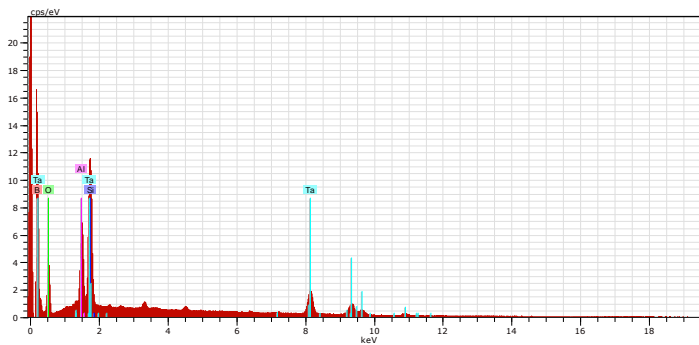


Figure 4.9: EDS spectrum for run 24.

Table 4: Atomic and weight percent for run 24.

El	AN	Series	C norm.	C Atom.	(1 Sigma)	
			[wt.%]	[at.%]	[wt.%]	
B	5	K-series	91586	93.38	96.43	10.60
O	8	K-series	32487	4.38	3.06	0.56
Al	13	K-series	63117	0.48	0.20	0.05
Si	14	K-series	86723	0.59	0.23	0.05
Ta	73	L-series	66342	1.16	0.07	0.05

4.2 Alpha- and Beta- Rhombohedral Boron

Crystalline alpha rhombohedral boron was first found in run 25 at a temperature of 950°C, using the higher purity BBr₃ from Alfa Aesar. The surface consisted of mostly speckled, shiny gray deposit with a few areas of light brown clusters, shown in Figure 4.10. Following the observations from previous runs, the speckled gray material is most likely glassy amorphous boron. The first appearance of light brown clusters could represent another form of amorphous boron. SEM images in Figure 4.11 show the microstructure of both materials, revealing smaller angular particulates within the shiny gray deposit which is assumed to be α -B. XRD confirmed the presence of α -B in addition to the consistently formed amorphous boron and TaB₂. As performed by David Rosenberg [21], the brown clusters were scraped off the bulk gray material and crushed separately for XRD. The resulting diffraction pattern in Figure 4.12 identified amorphous boron, TaB₂, and α -B. The material did not look crystalline under the scanning electron microscope, which implied that it was mostly made of either

amorphous boron or TaB_2 . To identify which compound contributed the most to the brown deposit, EDS was applied as shown in Figure 4.13. The atomic percent results, presented in Table 5, revealed a significantly larger amount of boron (96.91 at%) than tantalum (0.02 at%), concluding that the brown material was characteristic of amorphous boron.

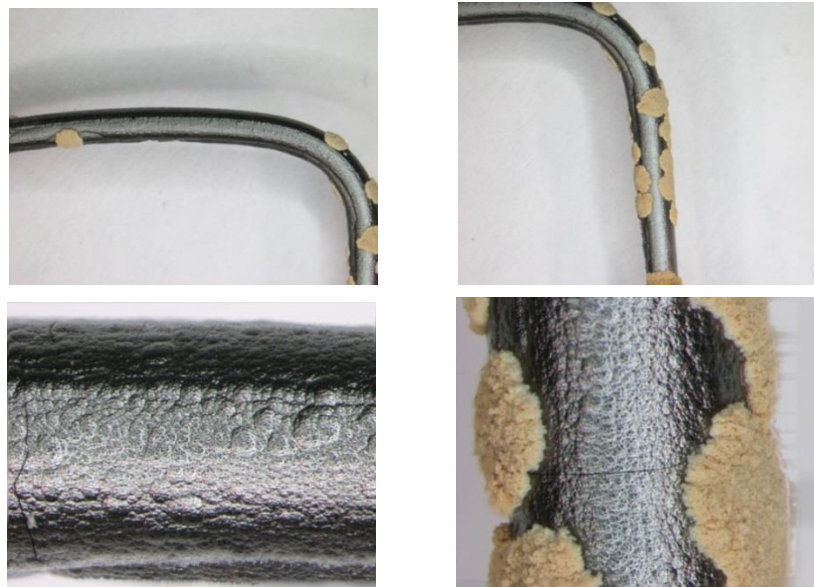


Figure 4.10: OM images of run 25 showing the speckled, shiny gray deposit and light brown clusters.

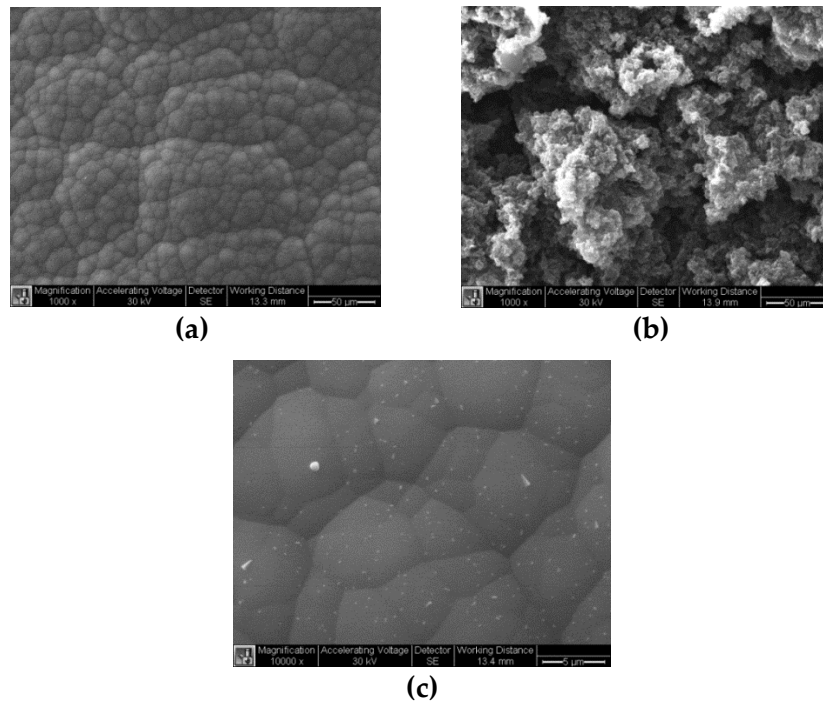


Figure 4.11: SEM images of run 25 showing the microstructure of the (a) speckled gray material and (b) light brown clusters (1000x). (c) A 10000x magnification reveals angular particulates, suggesting crystalline α -B consistent with XRD findings.

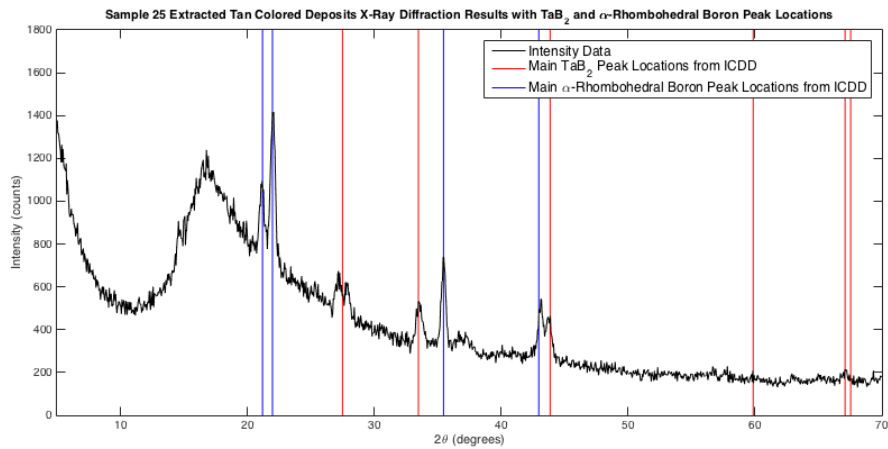


Figure 4.12: XRD pattern of the brown clusters found in run 25 showing amorphous boron, TaB₂, and α -B. XRD work was performed by David Rosenberg [21].

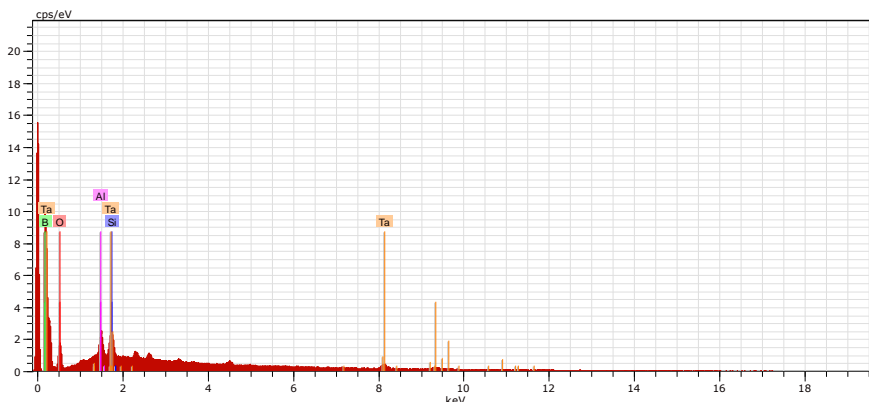


Figure 4.13: EDS spectrum for the brown clusters found in run 25.

Table 5: Atomic and weight percent of elements in the brown clusters found in run 25.

El	AN	Series	C norm.	C Atom.	(1 Sigma)	
			[wt.%]	[at.%]	[wt.%]	[wt.%]
B	5	K-series	49213	95.04	96.91	11.24
O	8	K-series	14725	4.23	2.92	0.59
Al	13	K-series	16100	0.23	0.09	0.04
Si	14	K-series	11357	0.14	0.06	0.03
Ta	73	L-series	9193	0.36	0.02	0.03

For run 26, two 5g ampules (99.99% purity from Aldrich) were used to maintain the same 10g amount of BBr_3 as run 25. The Aldrich BBr_3 was used due to manufacturer availability at the time and was assumed to provide the same quality as the Alfa Aesar BBr_3 . The experiment ran at an increased wire temperature of $975^\circ C$ in an attempt to form more α -B. The wire deposit showed a similar lumpy gray texture as run 25 but with less luster and no speckles (Figure 4.14). Comparing SEM images with run 25, run

26 had the same surface texture but with non-angular particulates (Figure 4.15). XRD revealed no α -B, only amorphous boron and TaB_2 .

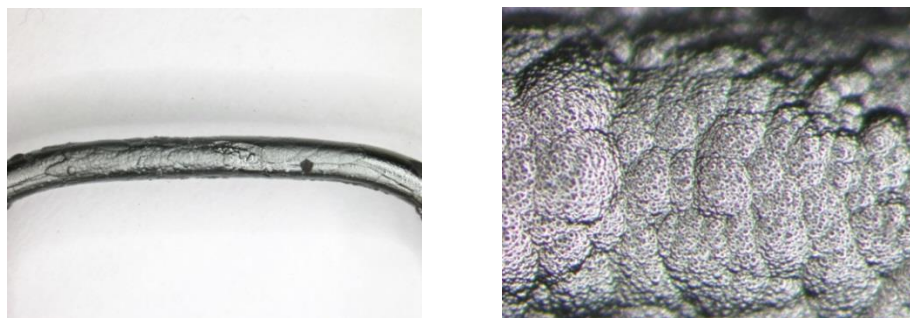


Figure 4.14: OM images of run 26 showing shiny gray deposit, similar to run 25 but with no speckled pattern.

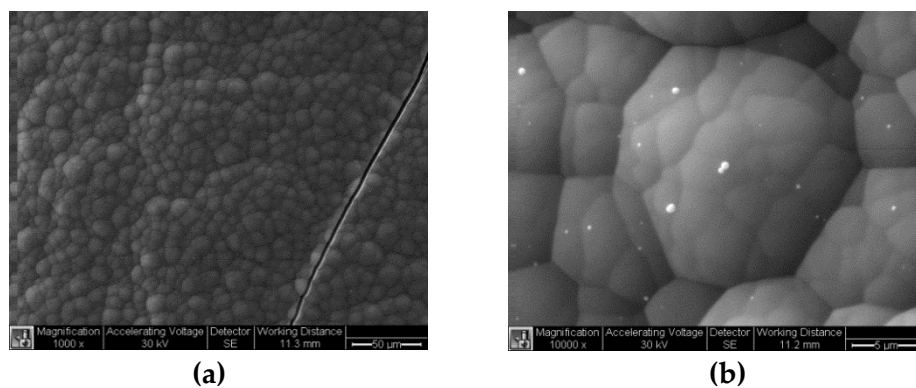


Figure 4.15: SEM images of run 26 at 1000x and 10000x magnification showing the (a) lumpy texture of the gray deposit and (b) smaller round particulates.

Another experiment was run at a higher temperature (1000°C) to test the temperature range for α -B formation. Run 27 used one 10g BBr_3 ampule from Alfa Aesar (99.999% purity). The accumulation of deposit on the wire was non-uniform throughout most of the run despite the relatively uniform layering in the end, so an average temperature was maintained using the optical pyrometer. Although no α -B was found

in run 26 at 975°C, α -B appeared in run 27 at 1000°C according to XRD results. In addition to α -rhombohedral boron, beta-rhombohedral boron made a first appearance among the sweep of temperatures. β -B has been reported to form at higher temperatures, so its appearance indicates the bound where α -B transitions into β -B. Following experiments would, therefore, be limited to temperatures no higher than 1000°C to maximize the amount of α -B formed. Other compounds found included amorphous boron and TaB_2 . OM and SEM images of the sample are shown in Figure 4.16 and Figure 4.17. The surface looked different compared to previous runs, covered with a rough brown layer and an underlying gray layer. SEM images showed the overlying texture to be similar to that of the brown clusters in run 25 (Figure 4.11(b)), indicating brown amorphous boron. Half of the wire deposit was crushed to perform XRD, and the leftover material on the wire was imaged again under the SEM for a closer look at the underlying material. The cross-section showed smoother texture but no definitive particulates of α -B as found in run 25. The α -B crystals were too small to view under an optical microscope.

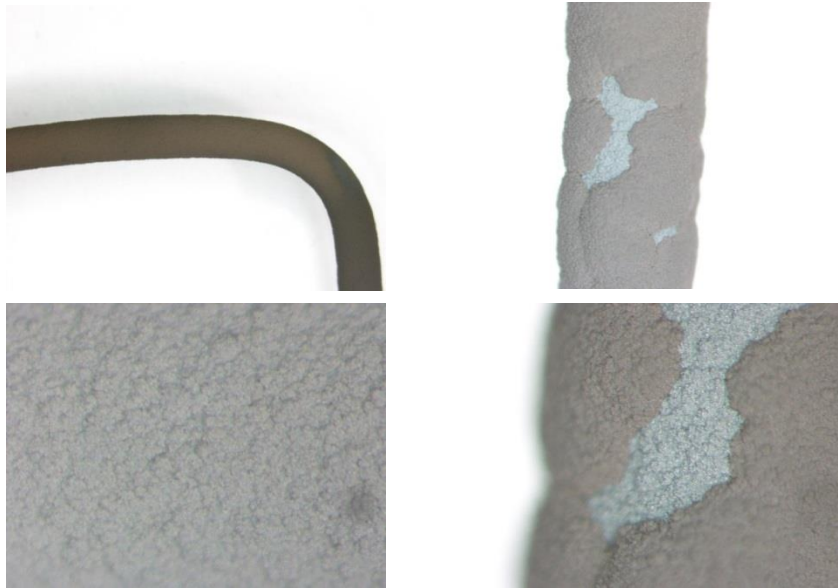
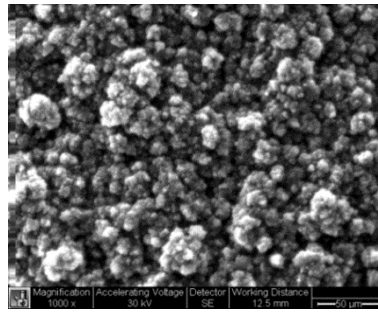
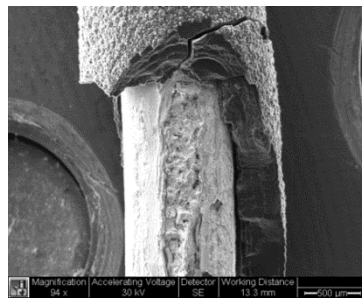


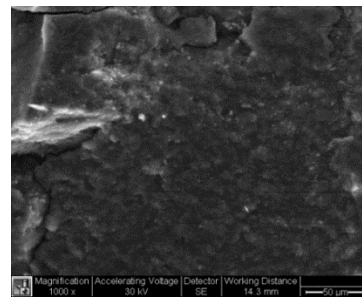
Figure 4.16: OM images of run 27 showing rough brown and gray deposits.



(a)



(b)



(c)

Figure 4.17: SEM images of run 27 showing (a) the microstructure of the overlying brown deposit (1000x), (b) a cross section of the deposit (94x), and (c) the texture of the underlying gray deposits revealed in the cross-section (1000x).

Run 28 was carried out at 975°C, retesting the conditions of run 26 but using the higher purity BBr₃ (99.999% from Alfa Aesar) as the reactant. The appearance of α-B at 950°C and 1000°C with 99.999% purity BBr₃ and the absence of α-B at 975°C with lower 99.99% purity BBr₃ might have implied that purity had a significant effect on α-B formation. However, even with the higher purity BBr₃, no α-B was formed at 975°C based on XRD analysis. β-B was found instead, indicating that the temperature may be too high for α-B formation. The underlying surface was shiny gray, as seen in Figure 4.18, and similar to run 26 (Figure 4.14); the texture shown by SEM in Figure 4.19 resembled those found in both runs 25 and 26 (Figure 4.15). Since α-B crystals were found within the similarly-shaped deposit in run 25, the lumpy shiny gray material is most likely glassy amorphous boron which provides a growth site for α-B. The overlying dull, gray material had a spherical cluster structure that was different from previous runs; it may be another form of TaB₂ or amorphous boron.

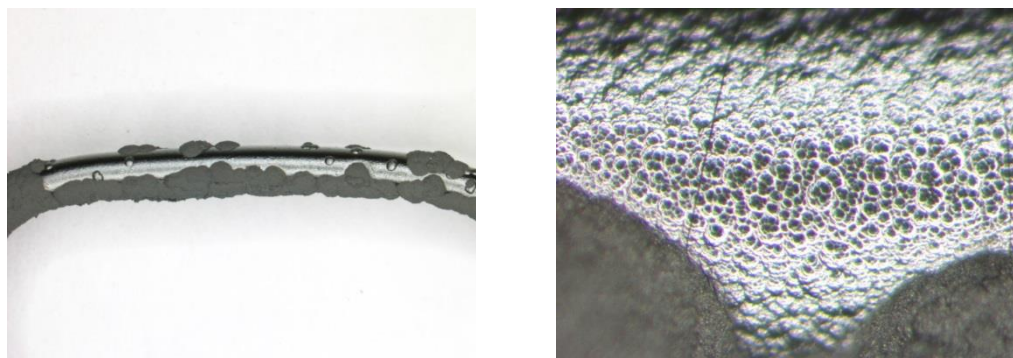
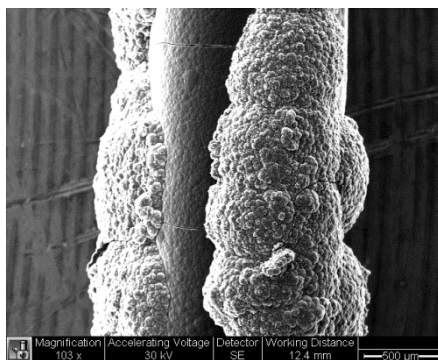
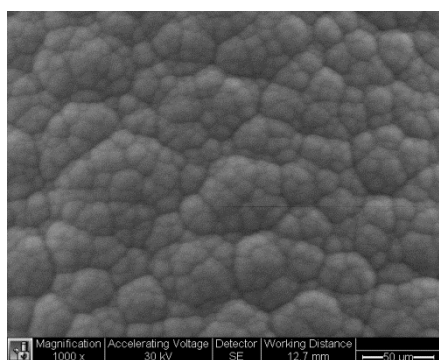


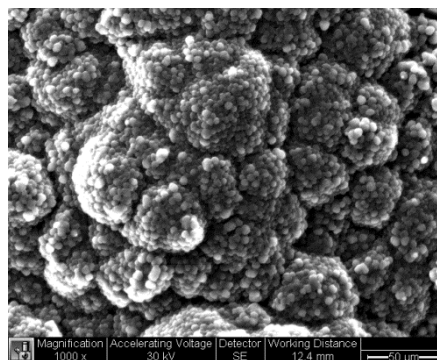
Figure 4.18: OM images of run 28 showing a shiny gray surface with an overlying layer of dull, darker gray material.



(a)



(b)



(c)

Figure 4.19: SEM images of run 28 showing (a) 103x overview of wire deposit, (b) lumpy texture of shiny gray material (1000x), and (c) spherical cluster structure of overlying dull gray material (1000x).

Run 29 was intended to reproduce α -B at 950°C, as previously seen in run 25. However, XRD results identified only TaB₂, amorphous boron, and β -B in the deposit. Both the morphology and appearance were different compared to sample 25. No α -B was found and the surface consisted of mostly rough, dull gray material instead of speckled, shiny gray material. See Figure 4.21 and Figure 4.22 for OM and SEM images of run 29. Slight metallic deposits were seen within the cracks of the surface, indicating an underlying glassy amorphous boron layer. The overall material had a nodule-like

microstructure which resembled that of the overlying layer in sample 28 (Figure 4.19(c)). Similarly, the dull gray material may suggest another form of TaB₂ or amorphous boron. The brown growths found on the surface of the deposit resemble the microstructure of the brown material found in runs 25 (Figure 4.11(b)) and 27 (Figure 4.17(a)), indicating brown amorphous boron. The absence of α -B could be attributed to insufficient purity within the system. The reactor, lines, and flask are thoroughly cleaned after each run, but it is possible that the gradual corrosion of the stainless steel reactor due to the hydrobromic acid byproduct is increasingly adding more impurities into the system. It is also important to note the uneven accumulation of deposit over the wire which causes non-uniform heating, as shown in Figure 4.20. An average temperature of 950°C was maintained for run 29, but nonetheless some areas of the deposit were hotter while other areas were colder. The hotter areas could have led α -B to transition into β -B.

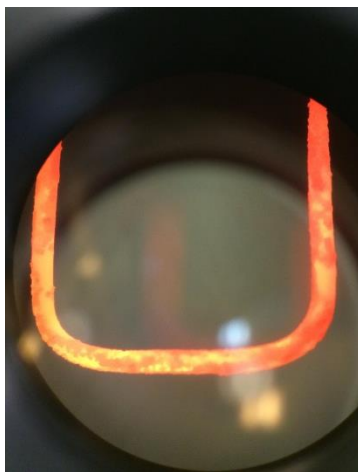


Figure 4.20: Heated wire during run 29 showing an uneven accumulation of deposit, resulting in a non-uniform heat distribution.

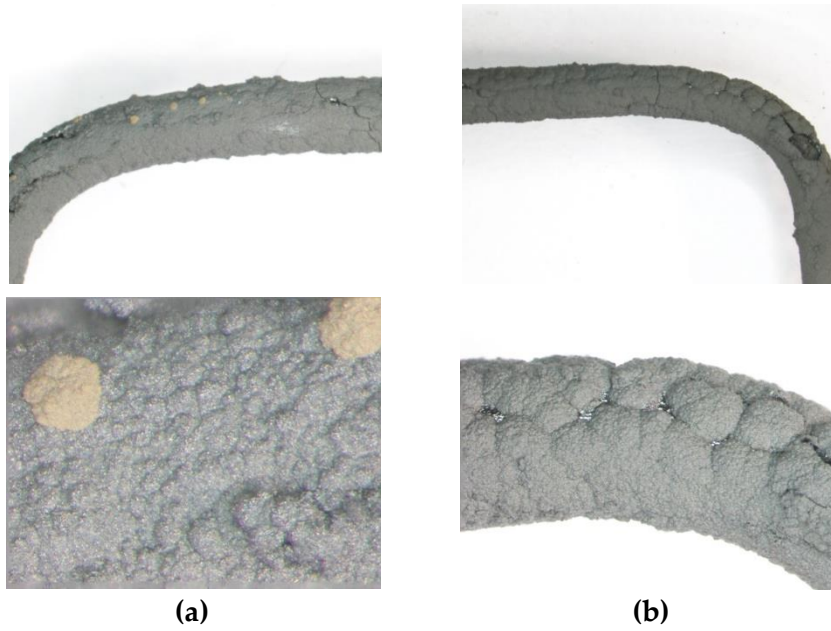


Figure 4.21: OM images of run 29 showing (a) an overall rough gray surface with a few brown growths and (b) underlying shiny boron, as seen through the cracks.

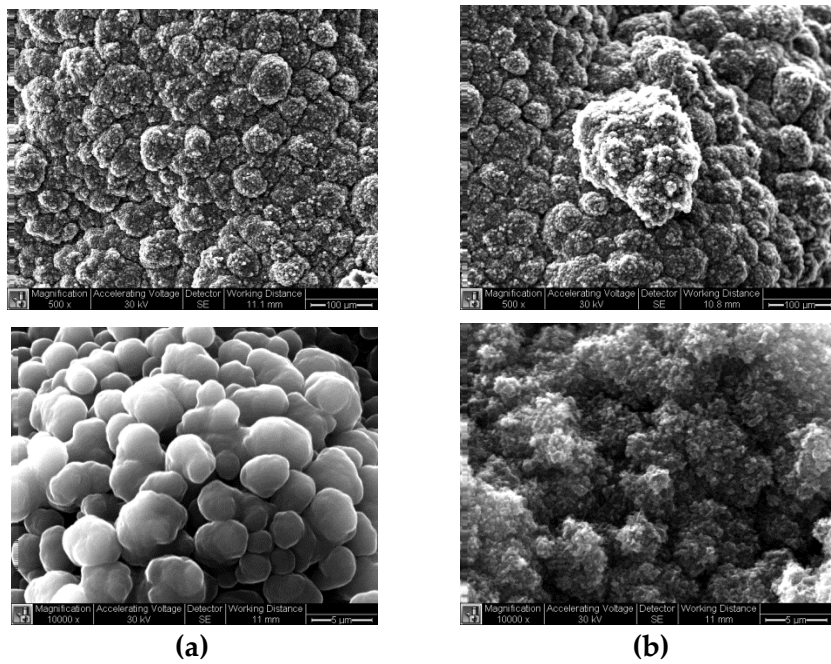


Figure 4.22: SEM images (500x and 10000x) of run 29 showing the microstructure of the (a) rough gray material and (b) brown growths.

4.3 High Vacuum Heating System

An attempt was made to grow α -B crystals from the experimental amorphous boron deposits by reheating the material in a vacuum system with 10,000 times lower vacuum than the current experimental setup. The first run in the high vacuum system used the wire from run 23 and heated the material to 1000°C for ~1 hour. XRD results did not show signs of α -B, only a significant increase in TaB₂. A second attempt was made with a sample that had trace amounts of α -B. The sample containing α -B from run 27 was heated at a deposit temperature of 950°C (wire temperature of 1150°C) and a vacuum of 4×10^{-3} microns for ~1 hour. Similar to the first run, only increased amounts of TaB₂ were found. Images of the high vacuum system are shown in Figure 4.23.

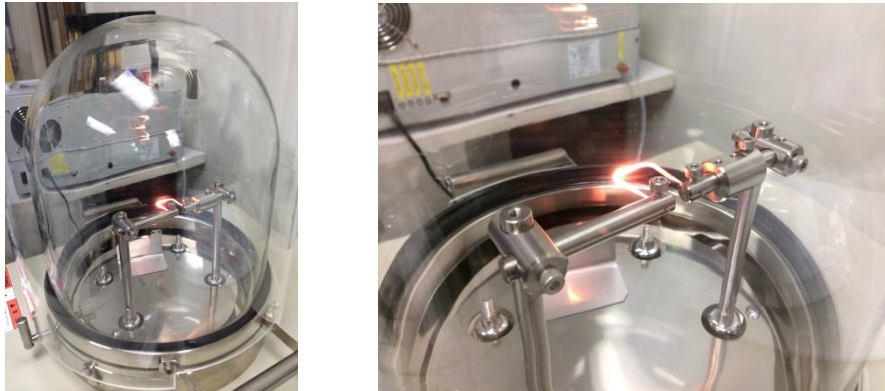


Figure 4.23: High vacuum system for reheating pyrolytic decomposition samples to test for increased α -B growth.

4.4 Boron Morphology Comparison

The SEM images of the deposit samples are compared to those found by other scientists experimenting with boron formation. Kuhlmann et al. [24] studied the optical

properties of amorphous boron, particularly two powder samples where one consisted almost entirely of amorphous boron and the other included 5-6% β -rhombohedral boron. Under the scanning electron microscope, the fully amorphous boron sample showed a spherical cluster microstructure similar to that of the rough gray material found in runs 28 and 29. Figure 4.24 shows side by side images of the amorphous boron sample by Kuhlmann et al. and sample 29. The amorphous boron was imaged in powder form whereas sample 29 was imaged as a solid deposit on the experimental wire. This may explain the more dispersed structure shown in the Kuhlmann et al. sample. The similarity in the overall structure between the samples implies that the gray material found in runs 28 and 29 is most likely amorphous boron rather than TaB_2 .

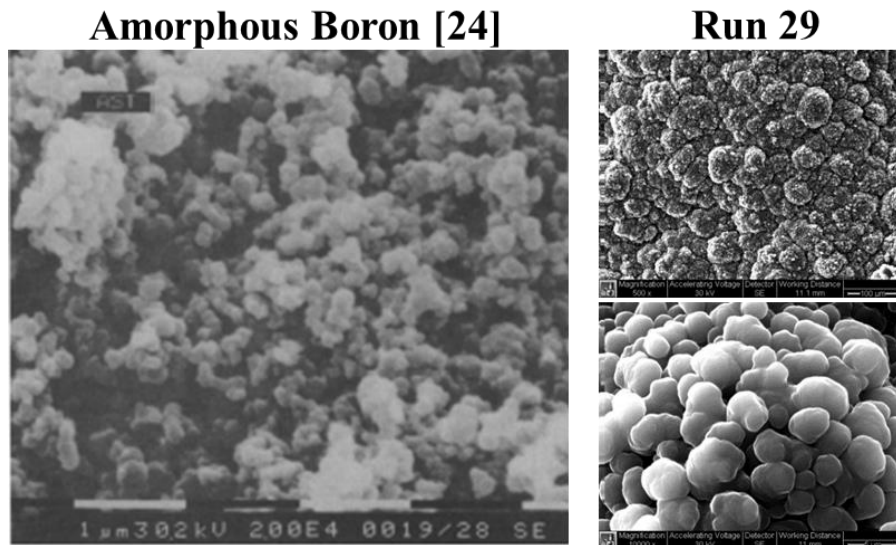


Figure 4.24: Comparison of amorphous boron sample by Kuhlmann et al. [24] and sample 29 from the boron tribromide pyrolysis experiment.

The other sample by Kuhlmann et al. [24] with 5-6% β -rhombohedral boron shows angular crystals within a similar amorphous boron structure, presented in Figure 4.25. Based on the image, the β -B seems to nucleate from the amorphous boron. Since this particular amorphous boron structure was found in the pyrolysis runs which formed β -rhombohedral boron (runs 28 and 29), we may conclude that this type of high temperature amorphous boron is a precursor characteristic to β -B formation.

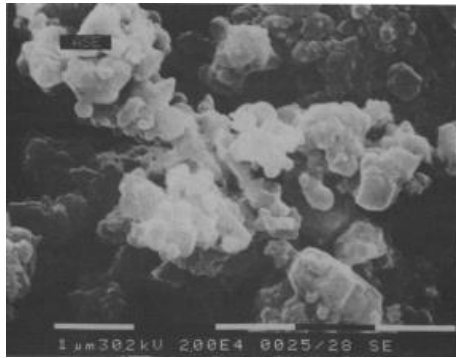


Figure 4.25: SEM image of amorphous boron sample with 5-6% β -B by Kuhlmann et al. [24], showing angular crystals within the spherical cluster structure.

Boron fibers were grown by Jan-Otto Carlsson [25] through the pyrolytic decomposition of boron trichloride. At $\sim 1180^{\circ}\text{C}$, amorphous boron formed with morphology similar to the lumpy gray material found in the boron tribromide pyrolysis runs 23 through 26 and run 28. The comparison shown in provides further verification that the majority of the material formed in the experiments was indeed amorphous boron rather than tantalum boride. Furthermore, Otto post-heated his samples in vacuum at $1000\text{-}1250^{\circ}\text{C}$ and produced α -rhombohedral boron crystals from the lumpy

amorphous boron, similar to how α -B crystals grew within the surface of the lumpy amorphous boron in run 25 (see). The lumpy structure is, therefore, characteristic of the lower temperature amorphous boron, including glassy boron, from which α -B may nucleate from given sufficient purity in the system.

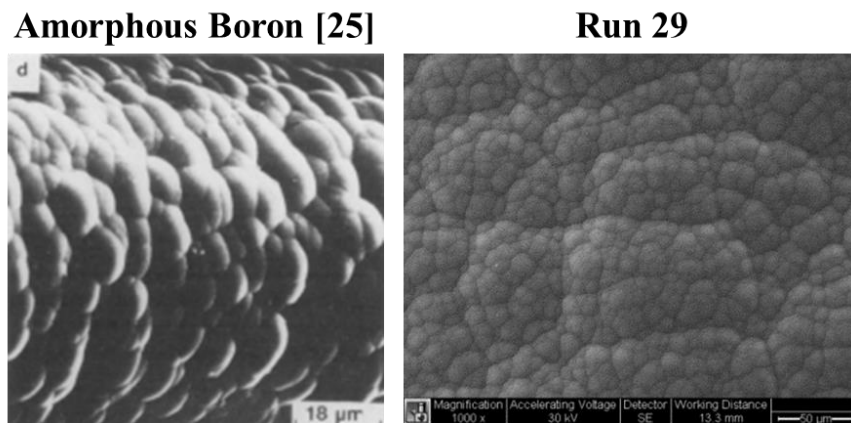


Figure 4.26: Comparison of amorphous boron sample by Otto [25] and sample 25 from the boron tribromide pyrolysis experiment.

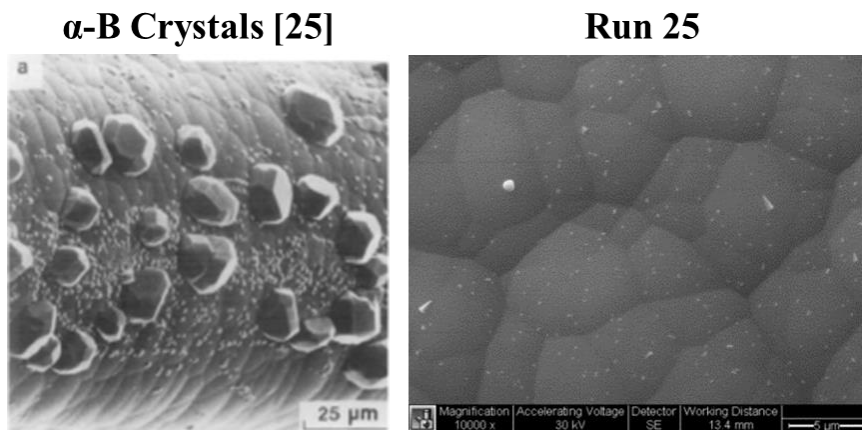


Figure 4.27: Comparison of alpha-rhombohedral boron growth from lumpy amorphous boron between sample by Otto [25] and sample 25.

Chapter 5: Conclusions

Pyrolytic decomposition of boron tribromide can produce alpha-rhombohedral boron, but to do so, two critical parameters must be met. First, the boron tribromide must be of extremely high purity. It was experimentally shown that 99.999% pure boron tribromide is necessary. 99.99% boron tribromide was found to only produce tantalum boride, amorphous boron, or beta-rhombohedral boron, but not alpha-rhombohedral boron. Since alpha-rhombohedral boron formation occurs in association with the crystallization of amorphous boron, the pyrolytic decomposition temperature must preferably be within the range 800°C to 1000°C. At higher temperatures, beta-rhombohedral boron is increasingly the phase that forms.

Different forms of amorphous boron may be classified according to their morphology and associated crystal growth. Lumpy gray boron encompasses glassy boron and is characteristic of lower temperature amorphous boron from which α -rhombohedral boron grows. There exists brown amorphous boron that is usually found as growths on top of lumpy gray amorphous boron. At higher temperatures, another type of gray amorphous boron characterized by a spherical cluster microstructure is found and may act as a site for β -rhombohedral boron growth.

Chapter 6: Future Work

The present work has produced only extremely small crystals, estimated to be between 0.2 μm and 1 μm in size. To increase the size of the alpha-rhombohedral boron crystals produced by the pyrolytic decomposition of boron tribromide, the stainless steel components used in this setup should be replaced by glass. Stainless steel corrodes in the hydrobromic acid formed by the interaction of boron tribromide with water vapor, and the resulting contamination of the deposited boron impedes the formation of $\alpha\text{-B}$, as shown by the fact that out of 29 total experimental runs, only two runs (run 25 and run 27) produced alpha-rhombohedral boron. This section discusses the modifications to the experimental setup design.

During post-run cleaning, corrosion was found in both the stainless steel 6-way cross reactor and stainless steel diaphragm valves connected by stainless steel Swagelok fittings. The reactor should be replaced by a 3-neck glass flask with large ports. The two side ports would include tapered glass joint feedthroughs, one to run Teflon tubing directly from the boron tribromide source to the reaction chamber and one to run Teflon tubing towards the vacuum pump. The side port downstream of the hydrogen flow would additionally have a glass valve attached to the feedthrough. The middle port will need a custom attachment piece to house the power feedthrough. This would consist of a custom machined tapered Teflon plug with two copper rods press fit through the plug. The stainless steel adapters that hold the tantalum wire would be replaced by a more

corrosion resistant material, such as tantalum, but would otherwise be of the same design with set screws. Glass valves would replace all of the stainless steel valves controlling the hydrogen flow into the reactor, including the two valves positioned at the side ports of the flask which houses the BBr_3 . This setup should help to provide unobstructed flow. If there is a build-up of hydrobromic acid or boron tribromide in the Teflon tubing or valves, the tubing can be replaced and the valves can be easily cleaned.

In future work, more parameters will be measured such as deposit diameter and hydrogen flow rate. This would allow for deposition rate estimates which may prove to be critical to α -rhombohedral boron formation, as shown in Otto's work with the pyrolytic decomposition of boron trichloride [25]. Moreover, longer heating times may be tested given that most experiments that have grown red boron have run for longer periods of time. The less corrosive setup should, nonetheless, provide better visual on what is happening in the setup to help troubleshoot problems and provide significantly increased purity for greater chances of growing red α -rhombohedral boron.

Bibliography

- [1] "Neutron Detectors: Alternatives to Using Helium-3," United States Government Accountability Office GAO-11-753, 2011.
- [2] F. H. Cocks and W. N. Simmons, "Red boron solid state detector," ed: Google Patents, 2015.
- [3] D. Emin, "Unusual properties of icosahedral boron-rich solids," *Journal of Solid State Chemistry*, vol. 179, pp. 2791-2798, 9// 2006.
- [4] G. V. Tsagareishvili and F. N. Tavadze, "Boron crystals: Preparation, structure and properties," *Progress in Crystal Growth and Characterization*, vol. 16, pp. 341-365, 1988/01/01 1988.
- [5] D. S. McGregor and J. Kenneth Shultis, "Spectral identification of thin-film-coated and solid-form semiconductor neutron detectors," *Nuclear Instruments and Methods in Physics Research Section A: Accelerators, Spectrometers, Detectors and Associated Equipment*, vol. 517, pp. 180-188, 1/21/ 2004.
- [6] D. S. McGregor, M. D. Hammig, Y. H. Yang, H. K. Gersch, and R. T. Klann, "Design considerations for thin film coated semiconductor thermal neutron detectors—I: basics regarding alpha particle emitting neutron reactive films," *Nuclear Instruments and Methods in Physics Research Section A: Accelerators, Spectrometers, Detectors and Associated Equipment*, vol. 500, pp. 272-308, 3/11/ 2003.
- [7] L. V. McCarty, J. S. Kasper, F. H. Horn, B. F. Decker, and A. E. Newkirk, "A NEW CRYSTALLINE MODIFICATION OF BORON," *Journal of the American Chemical Society*, vol. 80, pp. 2592-2592, 1958/05/01 1958.
- [8] F. H. Horn, "On the Crystallization of Simple Rhombohedral Boron from Platinum," *Journal of The Electrochemical Society*, vol. 106, pp. 905-906, October 1, 1959 1959.
- [9] F. Wald, "On the Stability of the Red α -Rhombohedral Boron Modification," *Electron Technology*, vol. 3, pp. 103-108, 1970.
- [10] W. Gao, "Crystal Growth of Alpha-Rhombohedral Boron," Master of Science, Chemical Engineering, Kansas State University, Manhattan, Kansas, 2010.

- [11] J. A. Ugai and N. E. Soloviev, "Methods of Preparation of α -Rhombohedral Boron," in *Boron and Refractory Borides*, V. I. Matkovich, Ed., ed Berlin, Heidelberg: Springer Berlin Heidelberg, 1977, pp. 227-240.
- [12] L. V. McCarty and D. R. Carpenter, "The Preparation of a New Crystalline Modification of Boron, and Notes on the Synthesis of Boron Triiodide," *Journal of The Electrochemical Society*, vol. 107, pp. 38-42, January 1, 1960 1960.
- [13] F. H. Horn, "Some Electrical and Optical Properties of Simple Rhombohedral Boron," *Journal of Applied Physics*, vol. 30, pp. 1611-1612, 1959.
- [14] E. Amberger and W. Dietze, "Synthesis of Red, α -Rhombohedral Boron," in *Boron: Volume 2: Preparation, Properties, and Applications*, G. K. Gaulé, Ed., ed Boston, MA: Springer US, 1965, pp. 1-7.
- [15] R. Naslain, J. Etourneau, and P. Hagenmuller, "Preparation of pure α - and β -rhombohedral boron. Alkali borides," *Electron Technology*, vol. 3, pp. 35-47, 1970 1970.
- [16] C. P. Talley, L. E. Line, and Q. D. Overman, "Preparation and Properties of Massive Amorphous Elemental Boron," in *Boron Synthesis, Structure, and Properties: Proceedings of the Conference on Boron*, J. A. Kohn, W. F. Nye, and G. K. Gaulé, Eds., ed Boston, MA: Springer US, 1960, pp. 94-104.
- [17] K. E. Bean and W. E. Medcalf, "Utilization of Boron Filaments in Vapor-Phase Deposition of Boron," in *Boron Synthesis, Structure, and Properties: Proceedings of the Conference on Boron*, J. A. Kohn, W. F. Nye, and G. K. Gaulé, Eds., ed Boston, MA: Springer US, 1960, pp. 48-58.
- [18] F. Wald and J. Bullitt, "Semiconductor Neutron Detectors," Tyco Laboratories, Inc. 1973.
- [19] R. S. Wagner and W. C. Ellis, "VAPOR-LIQUID-SOLID MECHANISM OF SINGLE CRYSTAL GROWTH," *Applied Physics Letters*, vol. 4, pp. 89-90, 1964.
- [20] J. P. Sitarik and W. C. Ellis, "Preparation and Morphology of Boron Filamentary Crystals Grown by the Vapor-Liquid-Solid Mechanism," *Journal of Applied Physics*, vol. 37, pp. 2399-2401, 1966.

- [21] D. Rosenberg, "X-Ray Diffraction Study of Boron Produced by Pyrolysis of Boron Tribromide," Master of Science, Mechanical Engineering and Material Science, Duke University, 2016.
- [22] D. Stokes, *Principles and practice of variable pressure/environmental scanning electron microscopy (VP-ESEM)*. Chichester, U.K.: Wiley, 2008.
- [23] *Scanning electron microscopy and x-ray microanalysis*. New York: Kluwer Academic/Plenum Publishers, 2003.
- [24] U. Kuhlmann, H. Werheit, T. Lundström, and W. Robers, "Optical properties of amorphous boron," *Journal of Physics and Chemistry of Solids*, vol. 55, pp. 579-587, 7// 1994.
- [25] J.-O. Carlsson, "Factors influencing the morphologies of boron deposited by chemical vapour deposition," *Journal of the Less Common Metals*, vol. 70, pp. 77-96, 3// 1980.